SUPPORTING INFORMATION FOR

Substrate Chemistry and Lattice Effects in Vapor Transport Growth of Vanadium Dioxide Microcrystals

Samuel T. White [1], Ellis A. Thompson [2], Peyton F. Brown [1], Richard F. Haglund [1*]*

[1]Physics and Astronomy Department, Vanderbilt University, Nashville, TN, 37212

[2]Department of Physics, University of Washington, Seattle, WA, 98195

[*]E-mail: richard.haglund@vanderbilt.edu, samuel.t.white@vanderbilt.edu

CONTENTS

S1: VO_2 Crystal Lattice and Phases

Figure S1 compares the unit cells of the M1, M2, and R phases of VO_2. The corresponding lattice parameters refenced throughout this work are presenting in Table S1.

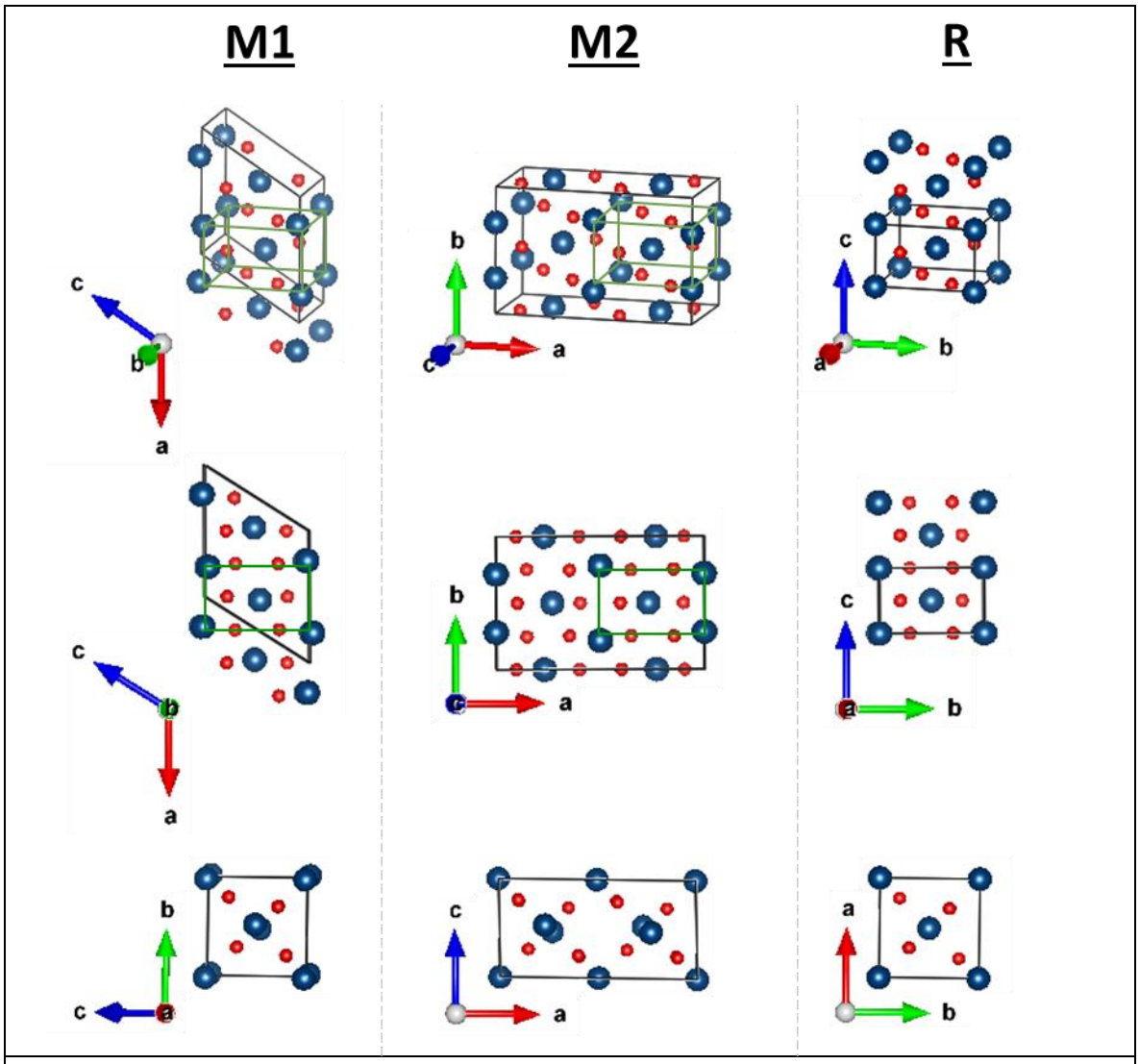

Figure S1: Schematic diagram of the VO_2 crystal structure in its M1, M2, and R phases. The unit cell for R is overlaid (in green) on the M1 and M2 structures as a guide to the eye.

Table S1: Lattice parameters for the M1, M2, and R VO_2 phases

Phase	Space Group	a (Å)	b (Å)	c (Å)	α(°)	β(°)	γ(°)	Ref.
M1	P 21/c	5.7517	4.5378	5.3825	90	122.646	90	[1]
M2	C 2/m	9.0600	5.8000	4.5217	90	91.850	90	[2]
R	P 42/m n m	4.5546	4.5546	2.8514	90	90	90	[3]

S2: Review of Progress in Vapor Transport Growth

The optimization of different parameters involved in vapor transport growth has progressed significantly. This method was first developed using VO_2 as a precursor[4-11], but V_2O_5 has become the standard precursor powder because of its lower melting point. VO_2 melts at 1967ºC, so using V_2O_5, which melts at about 690ºC, allows for a larger flux of vapor making for a more efficient growth[12-13]. Results of previous growths also show that varying growth conditions affects the morphology of the products. Higher temperatures tend to yield denser nanowires which may show directional growth or even larger nanoplatelets, whereas at lower temperatures, fewer, more loosely attached nanowires tend to form[8, 14]. In at least one study, use of a two-step method, wherein oxygen flow is introduced after the initial temperature ramp, yielded a higher density of nanowires as well[7].

Choice of substrate has been extensively explored as a parameter of crystal growth. Several studies have focused on the effects of lattice match, showing that varying the lattice structure of the substrate may alter the shape and orientation of VO_2 crystals. Table S2 summarizes substrates that have been used and how lattice match affects the crystals they yield. Generally, VO_2 crystals tend to grow along the rutile c-axis $[001]_R$ with facets along the low-surface-energy $\{110\}_R$ family of planes[11].

The most commonly used substrates for VO_2 crystal growth are silicon and silica. Vanadium dioxide crystals grown on pure SiO_2 tend to grow in specific directions depending on the cut used (with $[001]_R$ aligned to $\langle 2\bar{1}\bar{1}0\rangle_{SiO_2}$ on z-cut SiO_2[14] and to $\langle 1\bar{1}00\rangle_{SiO_2}$ on x-cut[12]). Silicon oxide on Si, pure Si, and Si_3N_4 have produced crystals with unique structural characteristics, but with random orientation in the plane of the substrate[4-5, 15-17]. Growth on TiO_2 (100) and TiO_2 (110) also results in crystals with different structural characteristics, having unique cross-sectional shapes, unusual crystal facets parallel to the substrate, and specific in-plane orientation[11]. Another widely-used substrate is Al_2O_3. In addition to varying structural characteristics, crystals grown on Al_2O_3 show definite evidence of preferred growth direction relative to the substrate, depending on the cut used[6, 10]. On c-cut, crystals grow at 60º angles relative to each other[6], whereas in r-cut and a-cut, crystals grow directionally out of plane relative to the substrate[10]. Across different crystalline substrates, the arrangement of atoms on the surface affects the shape and morphology of the crystals on a micron-scale.

Other substrate-dependent effects during crystal growth play a significant role in determining the properties of the resulting VO_2 crystals. In particular, chemical interactions between the substrates and vanadium precursors affect the growth mechanism. On substrates with SiO_2 at the surface, a eutectic region forms between newly formed VO_x droplets and VO_2 wires which dissolves a small amount of surrounding material, embedding the wire into the substrate. This facilitates unobstructed growth which leads to larger crystals[4, 17], and firmly clamps the crystals to the substrate. On TiO_2 substrates, the precursor vapor wets the surface during growth instead of forming droplets[17]. These observations show that interfacial interactions between liquid vanadium oxides and the substrate surface changes the growth mechanism on these substrates, which may result in different crystal morphologies. In addition, some crystals

grown on Al_2O_3 and SiO_2 have been shown to exist in the M2 phase at room temperature[7, 9, 18]. Although this has often been attributed to substrate-induced strain, the M2 phase persists in crystals removed from Al_2O_3 substrates (and thus relieved of substrate-induced strain). Moreover, the M2 phase has also been stabilized by aluminum doping[19], which suggests the possibility of a chemical effect.

Table S2: Summary of substrate effects on VO_2 crystal growth

Substrate	**Evidence of Lattice Match / Orientation**	**Evidence of Chemistry Effects**
SiO_2 z-cut $(0001)_{SiO_2}$	$[001]_R \parallel \langle 2\bar{1}\bar{1}0\rangle_{SiO_2}$ $\{110\}_R \parallel \{0001\}_{SiO_2}$ [14]	Molten V_2O_5 forms eutectic with SiO_2; eutectic layer facilitates growth; resulting VO_2 crystals embedded in SiO_2 [4, 17]
SiO_2 x-cut $(11\bar{2}0)_{SiO_2}$	$[001]_R \parallel \langle 1\bar{1}00\rangle_{SiO_2}$ $\{110\}_R \parallel \{11\bar{2}0\}_{SiO_2}$ [12]	
SiO_2 (amorphous) on Si	$\{110\}_R$ [4, 17] and $\{011\}_R$ [4] parallel to substrate; square-cross section[4, 16]; random orientation in plane[17]	
Si (w/ native oxide)	Random orientation in plane[6]	Si-assisted reduction: $2V_2O_5(l) + Si(s) \rightarrow 4VO_2(s) + SiO_2$ Leads to small, dense nuclei [17]
Si_3N_4	Rectangular cross section; $\{110\}_R$ parallel to substrate[5]	Higher density of nanowires compared to SiO_2 substrates [5]
GaN $(0001)_{GaN}$	In-plane orientation reflects hexagonal substrate symmetry [17]	Molten vanadia wets GaN surface [17]
TiO_2 $(110)_{TiO_2}$	Triangular cross section; exposed facets are $\{100\}_R$ planes; $[001]_R \parallel \langle 001\rangle_{TiO_2}$ $\{110\}_R \parallel \{110\}_{TiO_2}$ [11]	Molten vanadia wets TiO_2 surface [17]
TiO_2 $(100)_{TiO_2}$	Rectangular cross section; exposed facets are $\{100\}_R$ planes; $[001]_R \parallel \langle 001\rangle_{TiO_2}$ $\{100\}_R \parallel \{100\}_{TiO_2}$ [11]	
Al_2O_3 c-cut $(0001)_{Al_2O_3}$	Triangular cross-section[10-11], $[001]_R \parallel \langle 11\bar{2}0\rangle_{Al_2O_3}$ $\{100\}_R \parallel \{0001\}_{Al_2O_3}$ [10],	M2 phase stabilized at room temperature, attributed to strain effects[7, 9]
Al_2O_3 r-cut $(1\bar{1}02)_{Al_2O_3}$	Square-cross section[10]; growth axis out of plane, 60º relative to substrate surface, unique in-plane orientation[7, 10]	
Al_2O_3 a-cut $(11\bar{2}0)_{Al_2O_3}$	Square-cross section; growth axis out of plane, 3-fold in-plane orientation symmetry[10]	
Al_2O_3 m-cut $(10\bar{1}0)_{Al_2O_3}$	Nanoblocks and nanowires appear to exhibit preferred orientation [20]	
Al_2O_3 (amorphous) on SiO_2		Al-doping stabilizes M2-phase at room temperature [19]

S3: Sample and Precursor Loading

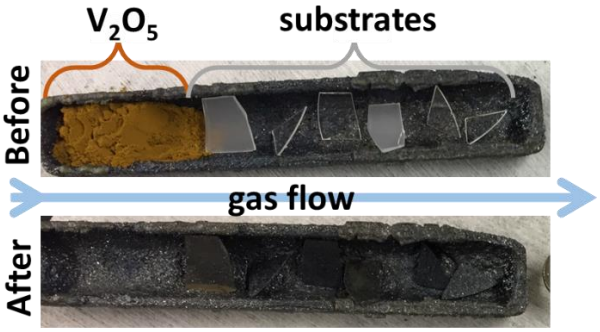

Figure S2: (top) Sample boats loaded with V_2O_5 precursor powder upstream, and growth substrates downstream. (bottom) After growth, the precursor has been consumed and substrates are covered with deposited material.

Figure S2 shows an example of the samples before and after the growth process. Orange vanadium pentoxide (V_2O_5) powder is loaded into one end of the boat, and growth substrates into the other. During the growth process, V_2O_5 vapor is carried to the substrates by a directional gas flow. After growth, the V_2O_5 is consumed and the substrates are darkened with a coating of VO_2 crystals.

S4: ETCH PITS IN SAPPHIRE

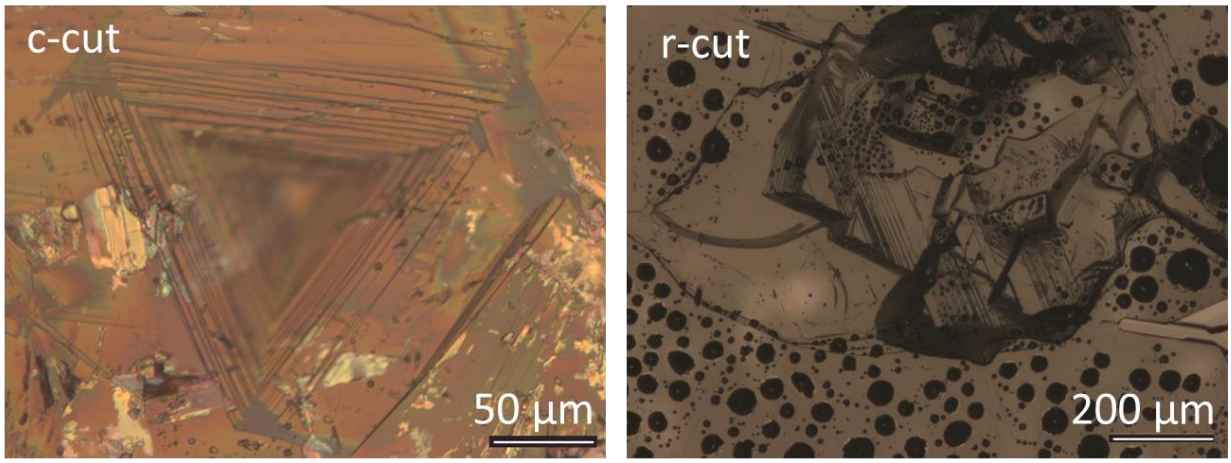

Figure S3: After crystal growth, etch pits can often be observed in the sapphire substrate.

After the growth process, pits can be observed in the sapphire substrate, examples of which are shown in Figure S3. These have a similar appearance to etch pits in sapphire[21], with a tendency to have stepped edges and to be shaped differently on different cuts, reflecting the difference in etch rates on different lattice planes. These pits are not observed on untreated substrates, or on substrates heated in the absence of V_2O_5 precursor. We attribute them to the corrosive action of molten V_2O_5, which has been used to etch Al_2O_3 surfaces[22-23].

S5: Examples of Large, Flat, Low-Aspect-Ratio Microcrystals on Sapphire

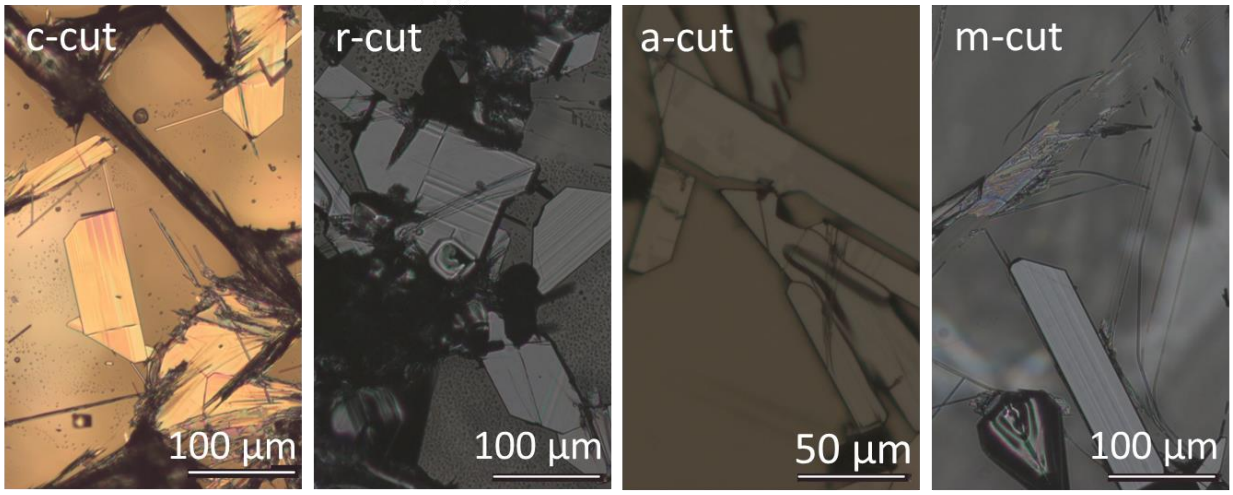

Figure S4: On each cut of sapphire, some crystals grow with large areas, low aspect ratios, and faces parallel to the substrate.

As discussed in the main text, both highly-oriented nanowires and un-oriented micro-platelets can be observed on each cut of sapphire. Examples of the latter are shown in Figure S4.

S6: ANALYSIS OF POLE FIGURES ON OTHER CUTS OF SAPPHIRE

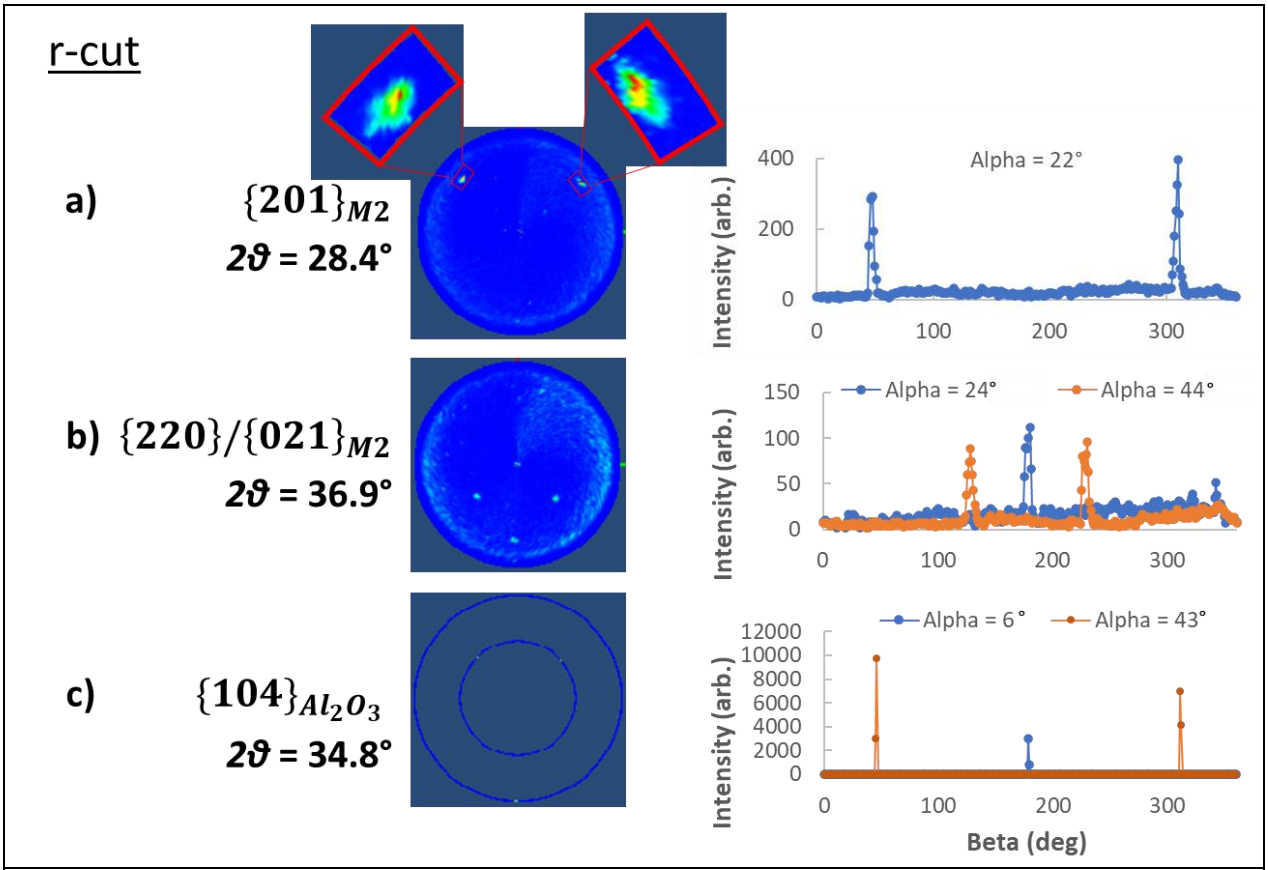

Figure S5: Additional XRD pole-figures (left) and constant-α cuts from the pole figures (right) were used in determining the VO_2 crystal orientation on r-cut sapphire. Higher-resolution scans (inset) show that the $\{201\}_{M2}$ peaks are single peaks rather than doublets.

On r-cut Al_2O_3, the $\{201\}_{M2} \equiv \{110\}_R$ family of planes shows one peak at α=90° ($\{110\}_R$ parallel to substrate) and two at α=22° with β=-2°±48°. The $\{220\}/\{021\}_{M2} \equiv \{011\}_R$ planes show four clear peaks: α=90°, α=45° with β=-1°±129°, and α=24° with β=180°. These four peaks correspond to the two $\{110\}_R$ peaks at α=22°. On the other hand, no $\{011\}_R$ peaks are observed that correspond to the $\{110\}_R$ peak at α=90°, which implies that these crystals have no in-plane orientation. Thus, some of the VO_2 crystals on r-cut Al_2O_3 have $\{110\}_R$ parallel to the substrate with no in-plane orientation, while others have $\{011\}_R$ parallel to the substrate with one unique in-plane orientation. To establish the substrate orientation, $\{104\}_{Al_2O_3}$peaks are observed at α=43° with β=-2°±48° and α=6° with β=178°. This establishes the orientation of the VO_2 crystals relative to the substrate, as listed in Table 2 of the main text.

Notably, this orientation is not the one that would yield the smallest lattice mismatch theoretically. If instead the orientation was $\langle 11\bar{1}\rangle_R \parallel \langle 0\bar{2}2\bar{1}\rangle_{Al_2O_3}$, the calculated mismatch would be only 0.3% (1.4%). This orientation is very close to that we observe, having only a ±2.5° shift in β; however, this would lead to a 5° peak splitting, which is not observed in our data, even with higher-resolution measurements (Figure S5a, insets).

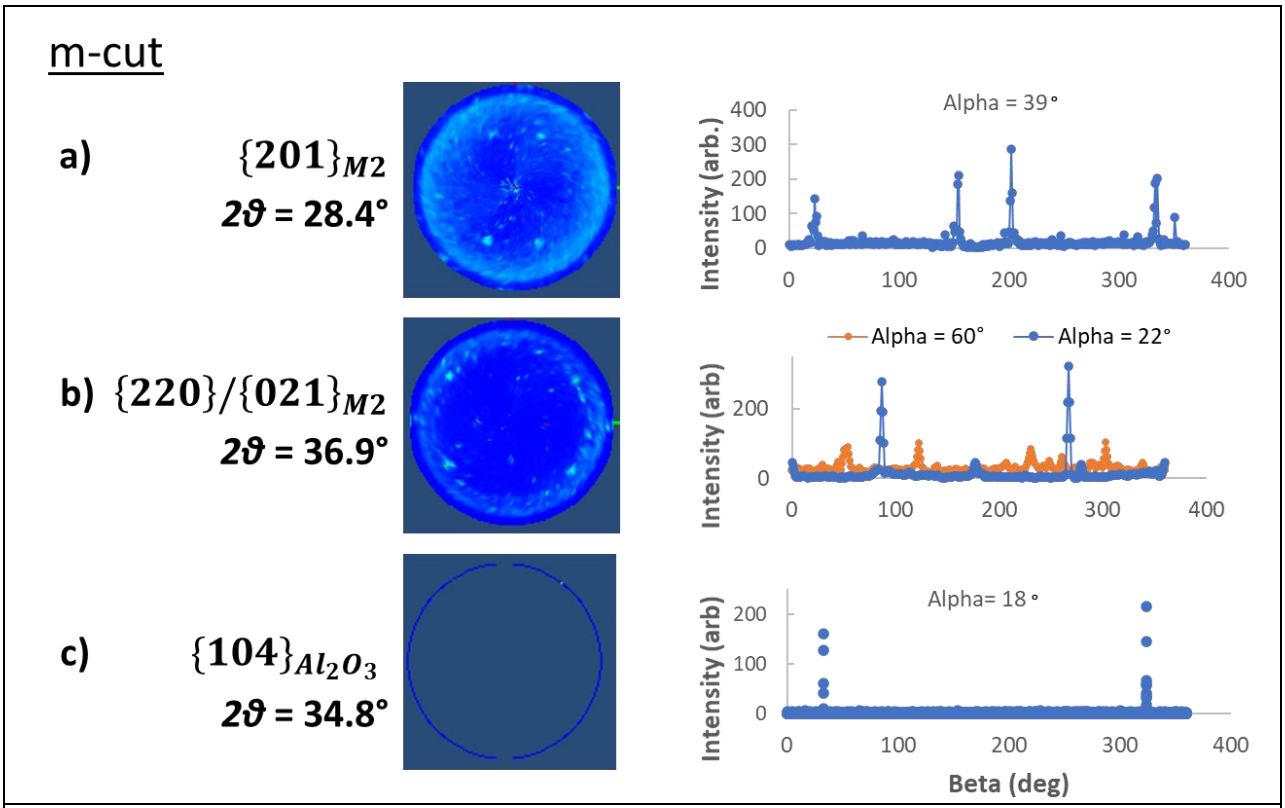

Figure S6: Additional XRD pole-figures (left) and constant-α cuts from the pole figures (right) were used in determining the VO_2 crystal orientation on m-cut sapphire.

On m-cut Al_2O_3, the $\{201\}_{M2} \equiv \{110\}_R$ family of planes shows one peak at α=90° ($\{110\}_R$ parallel to substrate) and four at α=39° with β=±24° or β=±155°. The $\{220\}/\{021\}_{M2} \equiv \{011\}_R$ planes show four clear peaks, all at α=21° with β=1°±54° or β=1°±125°. These four peaks correspond to the two $\{110\}_R$ peaks at α=39°, and arise from VO_2 crystals in two symmetry-equivalent orientations, which can be fully identified by comparison to the substrate $\{104\}_{Al_2O_3}$ peaks at α=18° and β=-2°±34° (see main text, Table 2). Once again, no $\{011\}_R$ peaks can be identified to correspond to the $\{110\}_R$ peaks at α=90°, indicating that the crystals with $\{110\}_R$ parallel to the substrate have no definite in-plane orientation.

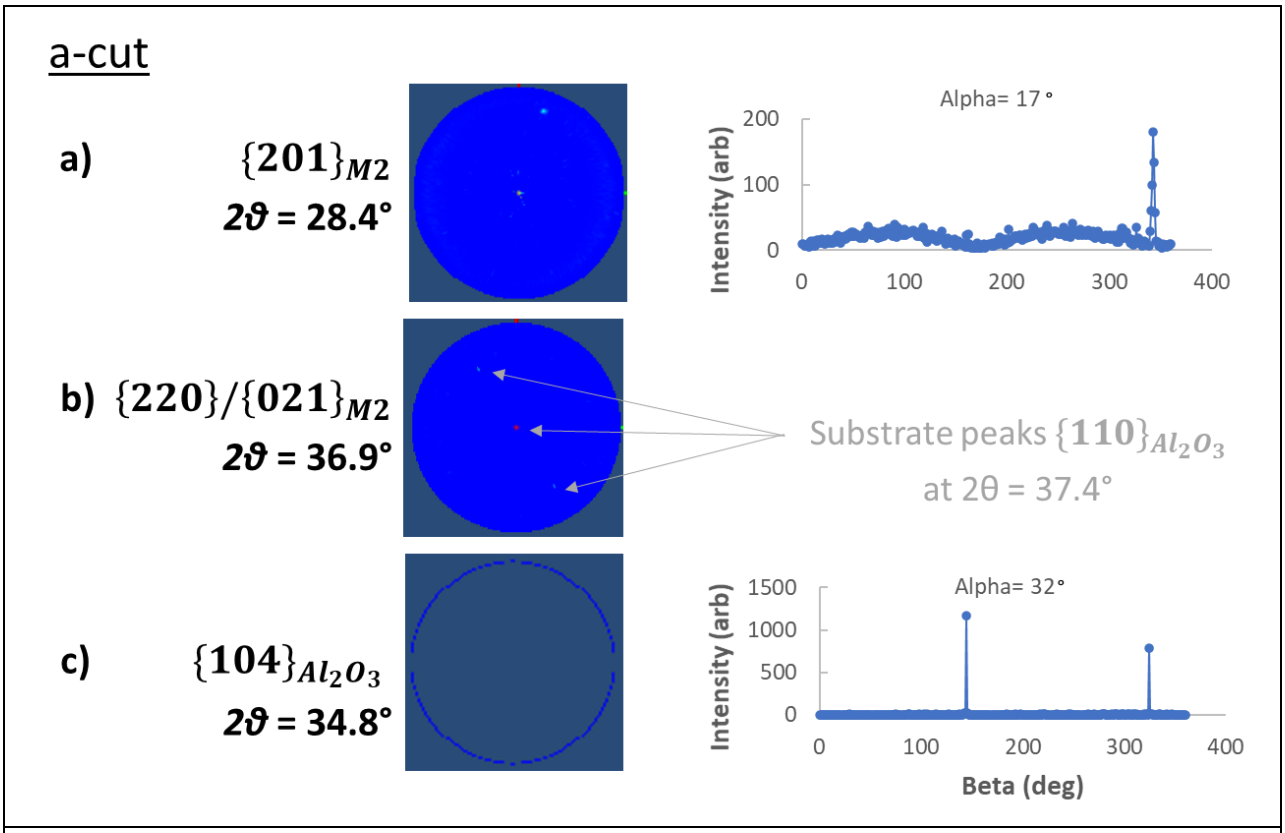

Figure S7: Additional XRD pole-figures (left) and constant-α cuts from the pole figures (right) were used in determining the VO_2 crystal orientation on m-cut sapphire. The peaks that appear in the $\{220\}/\{021\}_{M2}$ pole figure (at 2ϑ = 36.9°) are positioned where $\{110\}_{Al_2O_3}$ peaks (at 2θ = 37.4°) would be expected, and are likely the result of bleed-over from those reflections.

On a-cut Al_2O_3, the $\{201\}_{M2} \equiv \{110\}_R$ family of planes shows, as usual, one peak at α=90° ($\{110\}_R$ parallel to substrate), but only one other peak, at α=17° with β=-17°. Given the substrate symmetry, at least two peaks at α=17° would be expected for a sufficiently large sample of crystals; however, this sample was more sparsely covered with VO_2 than the others, and it may be that the corresponding symmetric peak was simply too weak to be observed. Similarly, no peaks are observed due to the $\{220\}/\{021\}_{M2} \equiv \{011\}_R$ family of planes. The peaks that do appear in the pole figure (Figure S6b) can be assigned to bleed-over from the (much more intense) $\{110\}_{Al_2O_3}$peaks which have a similar 2θ value. All of the $\{011\}_R$ peaks, being intrinsically less intense than the $\{110\}_R$, are simply too weak to be observed. However, to fully determine the orientation which produced the one $\{110\}_R$ peak at α=17° requires additional information. Standard θ-2θ measurements reveal all the VO_2 planes which are parallel to the substrate surface. Table S3 lists all the M2-VO_2 planes identified in θ-2θ measurements on a-cut Al_2O_3. Some of these may correspond to crystals with no in-plane orientation (as appears to be typical of the $\{201\}/\{20\bar{1}\}_{M2}$ planes), or to loose, randomly oriented crystals, but we can identify one that is consistent with $\{110\}_R$ peak at α=17°, which makes it possible to identify that orientation.

Table S3: M2 VO_2 peaks observed in θ-2θ measurements on a-cut sapphire
$\{201\}/\{20\bar{1}\}$
$\{220\}/\{021\}$
$\{400\}/\{002\}$
$\{401\}/\{202\}$

S7: Evidence that a YVO_4 Layer Underlies VO_2 Crystals on YSZ

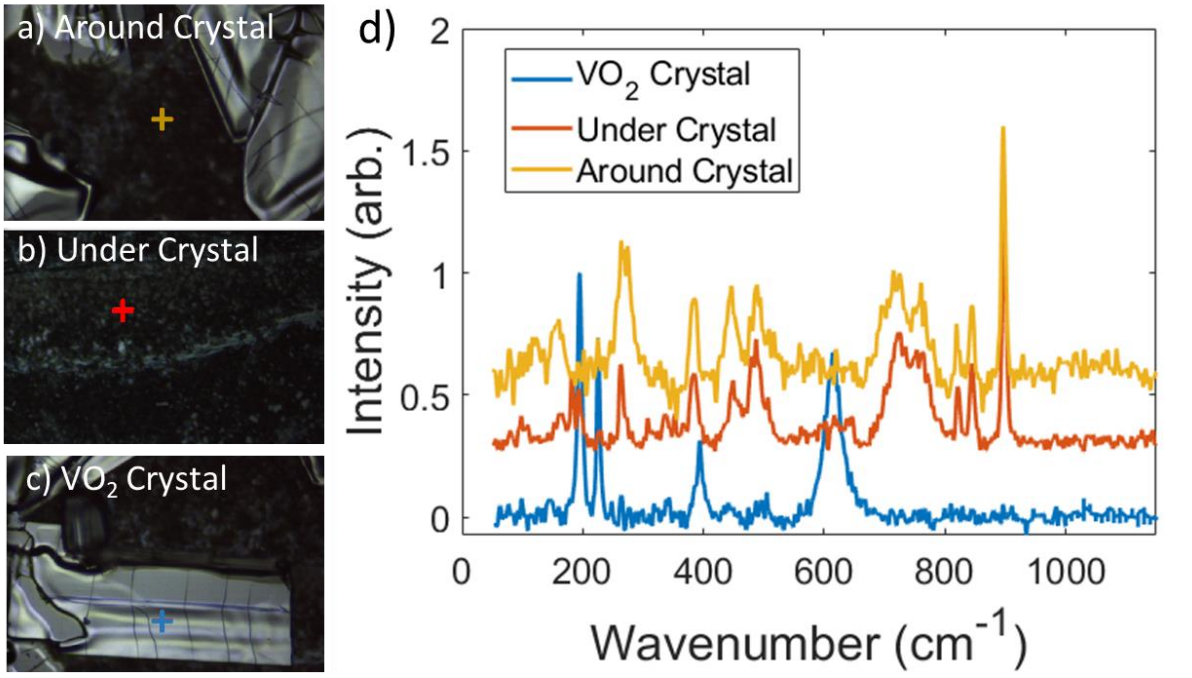

Figure S8: On YSZ, the substrate is covered by both VO_2 crystals (c) and a dark film composed of ZrO_2 and YVO_4 (a). When a VO_2 crystal is removed, the same film is observed beneath (b). Raman spectroscopy (d) shows that the material under (red) and around (yellow) the crystal is the same.

As discussed in the main text, YSZ substrates are covered in a dark, granular film after the crystal growth process. Raman spectroscopy showed this film to be composed of ZrO_2 and YVO_4. To determine whether this film covers the entire substrate or only that portion not occupied by VO_2 crystals, we remove a VO_2 crystal with adhesive tape and examine the material underneath. The crystal (Figure S7c) exhibits the characteristic Raman spectrum of VO_2 (Figure S7d, blue trace); once it has been removed, the area underneath it has the same visual appearance (Figure S7b) and Raman spectrum (Figure S7d, red trace) as the film that appears elsewhere on the exposed substrate (Figure S7a and S7d, red trace). This shows that the ZrO_2/YVO_4 film covers the entire substrate before VO_2 crystals form above it.

S8: POLE FIGURES FOR YVO_4, ZrO_2, ON YSZ

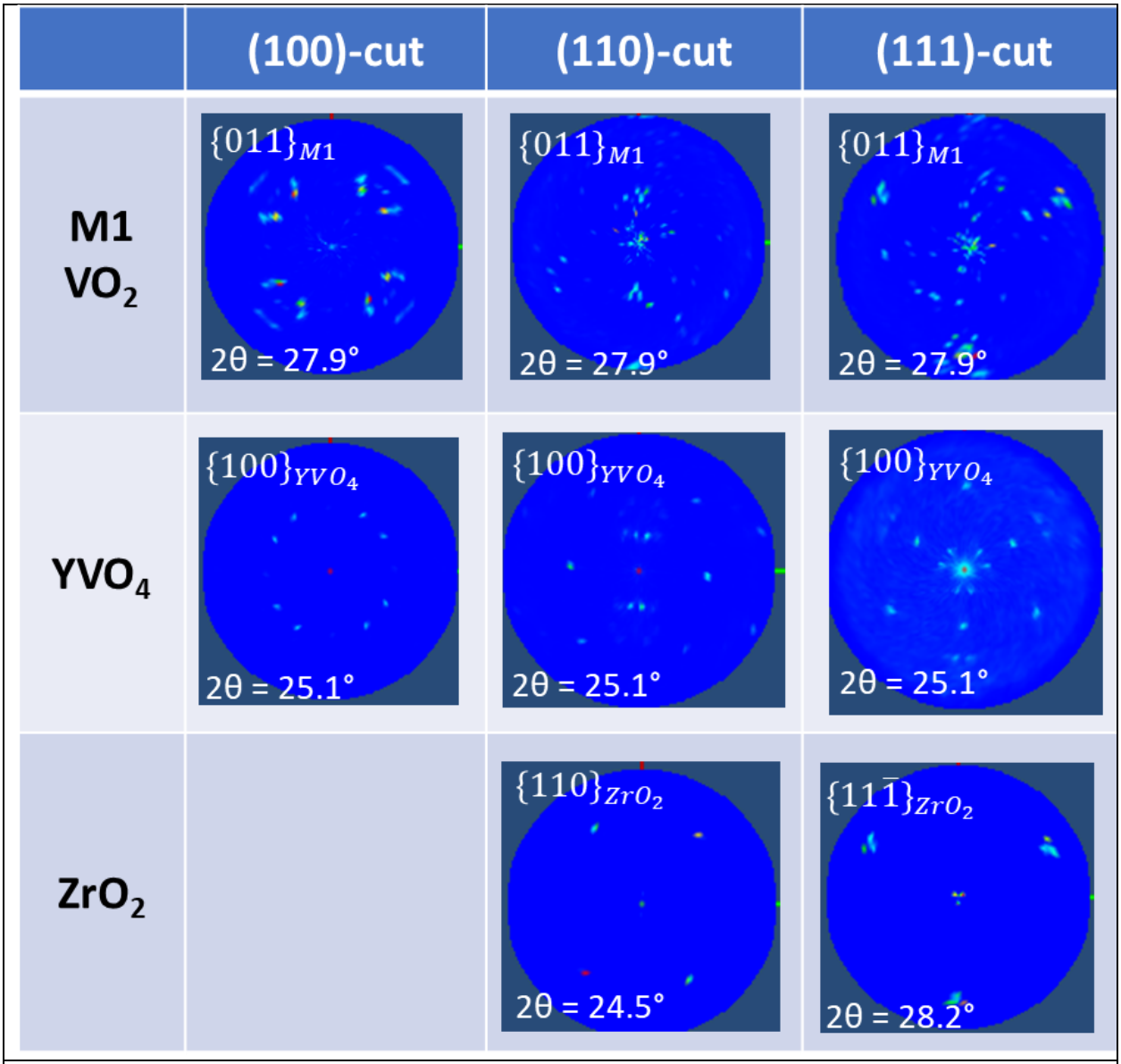

Figure S9: Additional pole figures for growths on all cuts of YSZ show evidence of preferred orientation for VO_2, YVO_4, and ZrO_2.

Figure S9 compares the pole figures for the VO_2 $\{011\}_{M1} \equiv \{1\bar{1}0\}_R$ family of planes to representative low-index planes belonging to YVO_4 and ZrO_2. Both YVO_4 and ZrO_2 exhibit sharp peaks in well-defined patterns, with a high degree of symmetry reflecting the symmetry of the substrate plane: 4-fold on (100)-cut, 2-fold on (110)-cut, and 3-fold on (111)-cut. This shows that the YVO_4 and ZrO_2 are highly-oriented, likely due to a heteroepitaxial relationship to the substrate and each other. Notably, the pole-figure patterns become progressively more complex from ZrO_2 to YVO_4 to VO_2. We hypothesize that atop the YSZ substrate is an yttria-

depleted ZrO_2 layer, heteroepitaxial to the substrate, but with multiple distinct orientations arising from its decreased symmetry. Above the ZrO_2 layer, the yttria reacts with V_2O_5 to form a YVO_4 layer, in turn oriented with respect to the ZrO_2. Multiple symmetry-allowed orientations lead to multiplicatively more peaks in the pole-figure pattern. VO_2 crystals grown on the YSZ layer in turn have preferred orientations relative to it. Finally, we note that since the $\{011\}_{M1}$ and $\{11\bar{1}\}_{ZrO_2}$ planes have similar 2θ values (27.9° and 28.2°, respectively) is it possible that some bleed-over from the more-intense ZrO_2 peaks contributes to the VO_2 pole figures.

S9: GROWTH RESULTS ON QUARTZ

Quartz is perhaps the most commonly-used and well-characterized substrate for VO_2 crystal growth by vapor-phase transport. As a baseline comparison for our crystals on other substrates, we present a sample grown on z-cut (0001) quartz. On this cut of quartz, crystals may exhibit a preferred orientation with six-fold symmetry[14], as noted above; and as on all SiO_2 substrates, VO_2 crystals will be embedded slightly in substrate due to formation of a eutectic during growth[17].

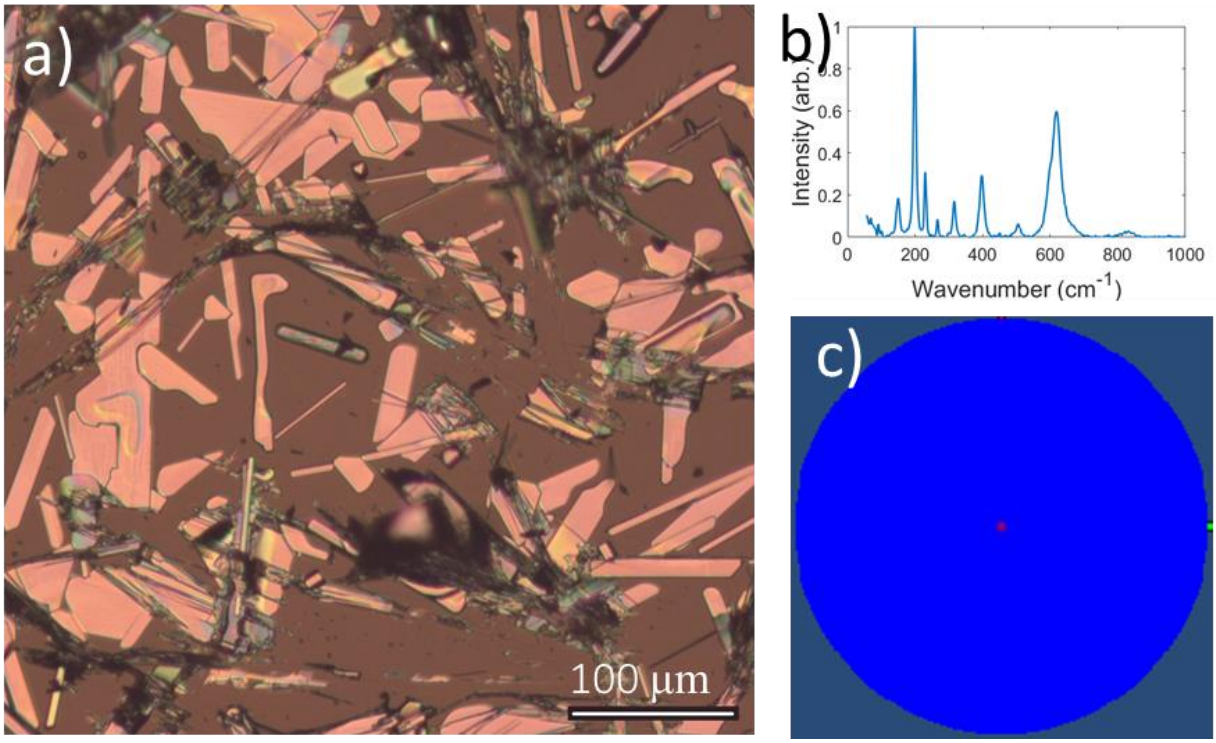

Figure S10: Examples of typical VO_2 crystals grown on quartz. Optical microscopy (a) shows that a variety of sizes and shapes appear, with no clear preferred orientation. Raman microscopy (b) shows the vast majority of crystals to be in the M1 phase at room temperature. Pole figure measurements (c) show that the $\{011\}_{M1}$ planes tend to be parallel to the substrate, but do not have a preferred orientation in-plane.

Figure S10 shows example data of our VO_2 crystals grown on z-cut quartz. Polarized optical microscopy (Figure S10a) shows that the crystals lie flat, with upper facets parallel to the substrate surface. The crystals are well adhered to the substrate—due to being embedded into the quartz, as mentioned above—and the substrate-induced strain results in complex ferroelastic twin domains (observed as light and dark mazelike patterns in the microscope image)[24]. There is no obvious preferred orientation, and our crystals are more reminiscent of those others have observed on SiO_2 thermal oxides on Si[4, 17], than the oriented nanowires observed on z-cut quartz[14]. As we observed in our sapphire growths, it is likely possible for both oriented

nanowires and non-oriented microplatelets to form, especially under different growth conditions. Raman microscopy (Figure S10b) shows that the majority of VO_2 crystals on quartz are in the M1 phase at room temperature, though some are in the T phase due to the influence of substrate strain.

Pole figure measurements (Figure S10c) show that the vast majority of $\{011\}_{M1} \equiv \{1\bar{1}0\}_R$ planes tend to be parallel to the substrate (α=90°). Replotting this figure on a log scale (Figure S11a) reveals an additional bright ring at α=45° with brighter spots appearing with a six-fold symmetry (reflective of the six-fold symmetry of the z-cut quartz substrate). Another bright ring in this figure at very low α is background noise present in all pole figures, usually too weak to appear on the scale used. The $\{200\}/\{21\bar{1}\}_{M1} \equiv \{011\}_R$ show peaks, of variable intensity, at α=27° with six-fold symmetry: β=12°+n*60° and β=48°+n*60° (n=0, 1, 2, 3, 4, 5). However, no VO_2 orientation can be identified to satisfy both $\{011\}_R$ at α=27° and $\{1\bar{1}0\}_R$ at either α=90° or α=45°. We conclude that most of our VO_2 crystals on quarts grow with $\{1\bar{1}0\}_R$ parallel to the substrate with no preferred in-plane orientation, while some crystals grow in at least two distinct orientations. Additional measurements will be required to identify the latter.

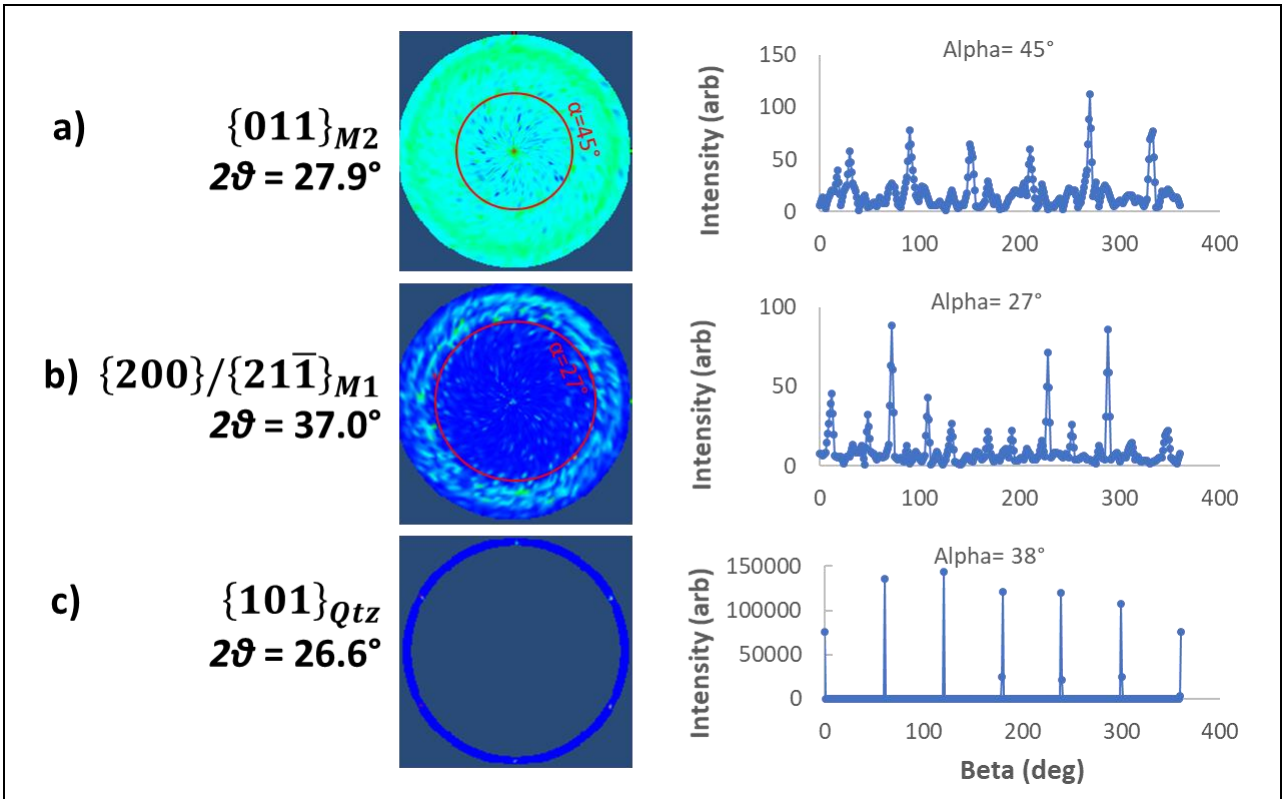

Figure S11: Pole figures (left) for quartz show bright rings, corresponding to crystals with a certain plane parallel to the substrate, but no in-plane orientation. Constant-alpha cuts (right) show some distinct peaks, suggesting a degree of preferred orientation; but no singe orientation can be identified to satisfy the peaks observed for both $\{011\}_{M2}$ and $\{200\}/\{21\bar{1}\}_{M1}$.

S10: Titanium Dioxide Substrate Properties

For this study, we chose two substrates that exemplify both chemical and lattice-matching effects in a well-understood case (Al_2O_3) as well as a novel one (YSZ). To similarly analyze all common VO_2 growth substrates is beyond the scope of this work, but one in particular deserves mention. Though more expensive, titanium dioxide (TiO_2) is commonly regarded as the best substrate for heteroepitaxial VO_2 growth because it has the same rutile crystal structure with very similar lattice parameters ($a_{R,TiO_2} = 4.593$Å and $c_{R,TiO_2} = 2.959$Å [25], compared to $a_{R,VO_2} = 4.555$Å and $c_{R,VO_2} = 2.851$Å [3]), and has produced highly-oriented films [26-27] and crystals [11]. Table S3 presents predicted lattice mismatch values for epitaxial VO_2 on several low-index planes of TiO_2. Compared to the values calculated for VO_2 on Al_2O_3 (Table 1 of the main text), these are for the most part comparable or better, with one notable exception: the percent lattice match for VO_2 on c-cut Al_2O_3 (according to the orientation we observed) is better than that on $\{110\}_{TiO_2}$ or $\{100\}_{TiO_2}$ (the two cuts of TiO_2 used previously for single-crystal VO_2 growth). Although this represents multi-domain heteroepitaxy on Al_2O_3 as opposed to single-domain on TiO_2, lattice match on sapphire suffices for our purposes.

Table S4: Predicted orientation and lattice match for VO_2 crystals grown on various cuts of TiO_2

Substrate Plane	Crystal Orientation	Lattice Mismatch ($\frac{d_{VO_2}-d_{TiO_2}}{d_{TiO_2}}$)	d_{VO_2} (Å)	d_{TiO_2} (Å)
$\{110\}_R \parallel \{110\}_{TiO_2}$	$[001]_R \parallel \langle 001\rangle_{TiO_2}$	-3.6%	2.851	2.959
	$[\bar{1}10]_R \parallel \langle \bar{1}10\rangle_{TiO_2}$	-0.8%	6.442	6.496
$\{100\}_R \parallel \{100\}_{TiO_2}$	$[001]_R \parallel \langle 001\rangle_{TiO_2}$	-3.6%	2.851	2.959
	$[010]_R \parallel \langle 010\rangle_{TiO_2}$	-0.8%	4.555	4.593
$\{001\}_R \parallel \{001\}_{TiO_2}$	$[100]_R \parallel \langle 100\rangle_{TiO_2}$	-0.8%	4.555	4.593
	$[010]_R \parallel \langle 010\rangle_{TiO_2}$	-0.8%	4.555	4.593
$\{011\}_R \parallel \{011\}_{TiO_2}$	$[100]_R \parallel \langle 100\rangle_{TiO_2}$	-0.8%	4.555	4.593
	$[01\bar{1}]_R \parallel \{01\bar{1}\}_{TiO_2}$	-1.6%	5.374	5.464

As with Al_2O_3 and YSZ, there is a possibility of chemical reaction between TiO_2 and V_2O_5. Studies on TiO_2-supported V_2O_5 catalysts show that at high temperatures vanadia catalyzes the TiO_2 anatase-to-rutile transition, and V^{4+} is incorporated into the rutile TiO_2 lattice, yielding $V_xTi_{1-x}O_2$ at the interface [28-30]. Also, V_2O_5 is reported to react with titania-stabilized zirconia (TiSZ) to produce $TiVO_4$ [31]. On the other hand, several corrosion studies on Ti-containing thermal barrier coatings suggest that TiO_2 is less reactive with vanadia than some other metal oxides, including alumina [32-34]. The possibility of chemical reactions occurring at the TiO_2-V_2O_5 interface during crystal growth certainly deserves further study, but sapphire provides a better example of substrate-vanadia reactions for this study.

There are few experimental studies of the TiO_2 surface energy, but computational studies predict values ranging from 0.3 to 1.8 J/m^2 for the $\{110\}_{TiO_2}$ plane, depending on the calculation

method, and higher for other planes [35-38]. The highest of these predicted values are larger than those used in our study, and might lead to good substrate wetting, as observed in one crystal growth study [17].

1. Longo, J. M.; Kierkega, P., A refinement of structure of VO_2. *Acta Chem. Scand.* **1970,** *24* (2), 420-426.
2. Ghedira, M.; Chenavas, J.; Marezio, M., Cation disproportionation and pairing in insulating T-phase of $V_{0.985}Al_{0.015}O_2$. *Journal of Physics C-Solid State Physics* **1977,** *10* (11), L309-L314.
3. McWhan, D. B.; Marezio, M.; Remeika, J. P.; Dernier, P. D., X-ray-diffraction study of metallic VO_2. *Phys. Rev. B* **1974,** *10* (2), 490-495.
4. Cheng, Y.; Wong, T. L.; Ho, K. M.; Wang, N., The structure and growth mechanism of VO_2 nanowires. *J. Cryst. Growth* **2009,** *311* (6), 1571-1575.
5. Guiton, B. S.; Gu, Q.; Prieto, A. L.; Gudiksen, M. S.; Park, H., Single-crystalline vanadium dioxide nanowires with rectangular cross sections. *J. Am. Chem. Soc.* **2005,** *127* (2), 498-499.
6. Kim, I. S.; Lauhon, L. J., Increased yield and uniformity of vanadium dioxide nanobeam growth via two-step physical vapor transport process. *Cryst. Growth Des.* **2012,** *12* (3), 1383-1387.
7. Kim, M. W.; Ha, S. S.; Seo, O.; Noh, D. Y.; Kim, B. J., Real-time structural and electrical characterization of metal-insulator transition in strain-modulated single-phase VO_2 wires with controlled diameters. *Nano Lett.* **2016,** *16* (7), 4074-4081.
8. Maeng, J.; Kim, T. W.; Jo, G.; Lee, T., Fabrication, structural and electrical characterization of VO_2 nanowires. *Mater. Res. Bull.* **2008,** *43* (7), 1649-1656.
9. Sohn, J. I.; Joo, H. J.; Ahn, D.; Lee, H. H.; Porter, A. E.; Kim, K.; Kang, D. J.; Welland, M. E., Surface-stress-induced mott transition and nature of associated spatial phase transition in single crystalline VO_2 nanowires. *Nano Lett.* **2009,** *9* (10), 3392-3397.
10. Sohn, J. I.; Joo, H. J.; Porter, A. E.; Choi, C. J.; Kim, K.; Kang, D. J.; Welland, M. E., Direct observation of the structural component of the metal-insulator phase transition and growth habits of epitaxially grown VO_2 nanowires. *Nano Lett.* **2007,** *7* (6), 1570-1574.
11. Wang, L. X.; Ren, H.; Chen, S.; Chen, Y. L.; Li, B. W.; Zou, C. W.; Zhang, G. B.; Lu, Y. L., Epitaxial growth of well-aligned single-crystalline VO_2 micro/ nanowires assisted by substrate facet confinement. *Cryst. Growth Des.* **2018,** *18* (7), 3896-3901.
12. Cheng, C.; Guo, H.; Amini, A.; Liu, K.; Fu, D.; Zou, J.; Song, H. S., Self-assembly and horizontal orientation growth of VO_2 nanowires. *Sci Rep* **2014,** *4*, 5456.
13. Cheng, C.; Liu, K.; Xiang, B.; Suh, J.; Wu, J. Q., Ultra-long, free-standing, single-crystalline vanadium dioxide micro/nanowires grown by simple thermal evaporation. *Appl. Phys. Lett.* **2012,** *100* (10), 103111.
14. Loffler, S.; Auer, E.; Weil, M.; Lugstein, A.; Bertagnolli, E., Impact of growth temperature on the crystal habits, forms and structures of VO_2 nanocrystals. *Appl. Phys. A-Mater. Sci. Process.* **2011,** *102* (1), 201-204.
15. Jiang, L. L.; Wei, M. D.; Ye, B. H.; Wei, K. M., VO_2 rods with a rectangular cross-section. *J. Cryst. Growth* **2008,** *310* (19), 4301-4304.
16. Lin, J.; Ji, H.; Swift, M. W.; Hardy, W. J.; Peng, Z. W.; Fan, X. J.; Nevidomskyy, A. H.; Tour, J. M.; Natelson, D., Hydrogen diffusion and stabilization in single-crystal VO_2 micro/nanobeams by direct atomic hydrogenation. *Nano Lett.* **2014,** *14* (9), 5445-5451.
17. Strelcov, E.; Davydov, A. V.; Lanke, U.; Watts, C.; Kolmakov, A., In situ monitoring of the growth, intermediate phase transformations and templating of single crystal VO_2 nanowires and nanoplatelets. *ACS Nano* **2011,** *5* (4), 3373-3384.
18. Jones, A. C.; Berweger, S.; Wei, J.; Cobden, D.; Raschke, M. B., Nano-optical investigations of the metal-insulator phase behavior of individual VO_2 microcrystals. *Nano Lett.* **2010,** *10* (5), 1574-1581.

19. Strelcov, E.; Tselev, A.; Ivanov, I.; Budai, J. D.; Zhang, J.; Tischler, J. Z.; Kravchenko, I.; Kalinin, S. V.; Kolmakov, A., Doping-based stabilization of the M2 phase in free-standing VO_2 nanostructures at room temperature. *Nano Lett.* **2012,** *12* (12), 6198-6205.
20. Choi, S.; Kim, B. J.; Lee, Y. W.; Yun, S. J.; Kim, H. T., Synethesis of VO_2 nanowire and observation of metal-insulator transition. *Jpn. J. Appl. Phys.* **2008,** *47* (4), 3296-3298.
21. Zhang, L. Y.; Sun, J. F.; Zuo, H. B.; Yuan, Z. Y.; Zhou, J.; Xing, D. W.; Han, J. C., Tridimensional morphology and kinetics of etch pit on the {0001} plane of sapphire crystal. *J. Solid State Chem.* **2012,** *192*, 60-67.
22. Katz, J. D.; Hurley, G., Etching alumina with molten vanadium pentoxide. *J. Am. Ceram. Soc.* **1990,** *73* (7), 2151-2152.
23. Safdar, M.; Frischat, G. H.; Salge, H., Etching of Al_2O_3 surfaces with molten V_2O_5. *J. Am. Ceram. Soc.* **1974,** *57* (2), 106-106.
24. Tselev, A.; Strelcov, E.; Luk'yanchuk, I. A.; Budai, J. D.; Tischler, J. Z.; Ivanov, I. N.; Jones, K.; Proksch, R.; Kalinin, S. V.; Kolmakov, A., Interplay between ferroelastic and metal-insulator phase transitions in strained quasi-two-dimensional VO_2 nanoplatelets. *Nano Lett.* **2010,** *10* (6), 2003-2011.
25. Burdett, J. K.; Hughbanks, T.; Miller, G. J.; Richardson, J. W.; Smith, J. V., Structural electronic relationships in inorganic solids - powder neutron-diffraction studies of the rutile and anatase polymorphs of titanium-dioxide at 15 and 295-K. *J. Am. Chem. Soc.* **1987,** *109* (12), 3639-3646.
26. Muraoka, Y.; Ueda, Y.; Hiroi, Z., Large modification of the metal-insulator transition temperature in strained VO_2 films grown on TiO_2 substrates. *J. Phys. Chem. Solids* **2002,** *63* (6-8), 965-967.
27. Sambi, M.; Sangiovanni, G.; Granozzi, G.; Parmigiani, F., Growth and the structure of epitaxial VO_2 at the TiO_2(110) surface. *Phys. Rev. B* **1997,** *55* (12), 7850-7858.
28. Vejux, A.; Courtine, P., Interfacial reactions between V_2O_5 and TiO_2 (anatase) - role of structural-properties. *J. Solid State Chem.* **1978,** *23* (1-2), 93-103.
29. Saleh, R. Y.; Wachs, I. E.; Chan, S. S.; Chersich, C. C., The interaction of V_2O_5 with TiO_2(anatase) - catalyst evolution with calcination temperature and o-xylene oxidation. *J. Catal.* **1986,** *98* (1), 102-114.
30. Haber, J.; Nowak, P., A catalysis related electrochemical study of the V_2O_5/TiO_2 (rutile) system. *Langmuir* **1995,** *11* (3), 1024-1032.
31. Habibi, M. H.; Guo, S. M., The hot corrosion behavior of plasma sprayed zirconia coatings stabilized with yttria, ceria, and titania in sodium sulfate and vanadium oxide. *Mater. Corros.* **2015,** *66* (3), 270-277.
32. Liu, H.; Cai, J.; Zhu, J. H., Hot corrosion behavior of $BaLa_2Ti_3O_{10}$ thermal barrier ceramics in V_2O_5 and $Na_2SO_4 + V_2O_5$ molten salts. *Coatings* **2019,** *9* (6), 351.
33. She, Y. J.; Guo, Y. W.; Tan, Z. X.; Liao, K., $Na_2SO_4 + V_2O_5$ corrosion behavior of $BaNd_2Ti_3O_{10}$ for thermal barrier coating applications. *Coatings* **2020,** *10* (9), 901.
34. Singh, G.; Kumar, S.; Kumar, R., Comparative study of hot corrosion behavior of thermal sprayed alumina and titanium oxide reinforced alumina coatings on boiler steel. *Mater. Res. Express* **2020,** *7* (2), 026527.
35. Barnard, A. S.; Zapol, P.; Curtiss, L. A., Modeling the morphology and phase stability of TiO_2 nanocrystals in water. *J. Chem. Theory Comput.* **2005,** *1* (1), 107-116.
36. Labat, F.; Baranek, P.; Adamo, C., Structural and electronic properties of selected rutile and anatase TiO_2 surfaces: An ab initio investigation. *J. Chem. Theory Comput.* **2008,** *4* (2), 341-352.
37. Lazzeri, M.; Vittadini, A.; Selloni, A., Structure and energetics of stoichiometric TiO_2 anatase surfaces. *Phys. Rev. B* **2001,** *63* (15), 155409.
38. Okeke, G.; Hammond, R. B.; Antony, S. J., Effects of heat treatment on the atomic structure and surface energy of rutile and anatase TiO_2 nanoparticles under vacuum and water environments. *Chem. Eng. Sci.* **2016,** *146*, 144-158.